

EXAFS study of mechanical-milling-induced solid-state amorphization of Se

Y.H. Zhao ^{a,*}, K. Lu ^a, T. Liu ^b

^a *Shenyang National Laboratory for Materials Science, Institute of Metal Research, Chinese Academy of Sciences, Shenyang 110016, People's Republic of China*

^b *Synchrotron Radiation Laboratory, Institute of High Energy Physics, Chinese Academy of Sciences, Beijing 100039, People's Republic of China*

Received 6 March 2002; received in revised form 1 December 2003

Abstract

Complete solid-state amorphization has been realized in elemental selenium by means of mechanical milling of crystalline Se powder. Extended X-ray-absorption fine-structure measurements (EXAFS) indicated that the amorphization process of crystalline Se was accompanied with a decrease of the nearest neighboring coordination number and the bond length, and the increase of the Debye–Waller factor. Combined with the previous study, we conclude that the mechanical milling results in the strengthening of intra-chain and weakening of inter-chain interactions of Se during amorphization. Compared to the structure of the as-quenched amorphous Se, the first nearest neighbor coordination number of the as-milled amorphous Se becomes smaller, while the Debye–Waller factor is larger, which is caused by the milling process.

© 2004 Published by Elsevier B.V.

PACS: 61.10.Ht; 61.66.Bi; 64.60.Cn; 81.20.Wk

1. Introduction

Currently, ball-milling-induced solid-state amorphization (SSA, or crystalline to amorphous phase transformation) receives considerable scientific interest, because it may offer a possibility to produce technologically useful bulk amorphous materials [1]. To date the SSA process can be induced by mechanical alloying (MA) of mixtures of pure elemental crystalline powders [2–6] or mechanical milling (MM) of crystalline intermetallic compounds [7–11] and pure covalently bonded elements [12–17]. In the former case, the amorphization is attributed to the solid-state interdiffusion reaction, the kinetics of which is controlled by the excess point and lattice defects [5]. In the latter case, MM induces accumulations of lattice imperfections and/or chemical disorders that raise the free energy of the milled system

above that of amorphous state, leading to a collapse of the crystalline structure [3].

Among the pure elements Si [12–14], Ge [15] and Se [16,17], of which SSA can be induced by MM, trigonal Se (t-Se) is the only one that can be fully amorphized due to its special molecular structure. As shown in the inset [18] in Fig. 1, t-Se consists of helical $[-Se-]_n$ molecular chains, Se atoms in the molecular chain are bonded with strong covalent bonds (such as A–B bond), and atoms on the adjacent Se molecular chains (such as A–A* bond) are bonded with weak Van der Waals forces [19]. In previous work, quantitative X-ray diffraction (XRD) measurements on MM-induced SSA of t-Se indicated that the amorphization onset corresponds to critical values of crystallite size and expansion of lattice parameter a (the distance between the neighboring $[-Se-]_n$ molecular chains), as well as a maximum microstrain [20]. Infrared and Raman spectroscopy measurements revealed that the as-milled amorphous Se (am-Se) is mainly composed of the disordered $[-Se-]_n$ polymeric chains [21]. These results suggest that the MM process introduced lattice imperfections into the inter-chain of $[-Se-]_n$ molecules, and when the accumulation

* Corresponding author. Present address: Los Alamos National Laboratory, MST-STC, G755, Los Alamos NM 87545, USA. Tel.: +1-505 665 6774; fax: +1-505 667 2264.

E-mail address: zhao@lanl.gov (Y.H. Zhao).

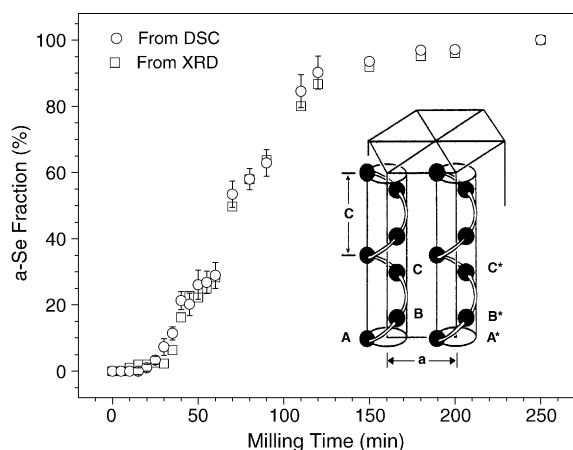


Fig. 1. Milling time dependence of the amorphous Se fraction obtained from X-ray diffraction (empty squares) and differential scanning calorimeter (empty circles) analyses [20] and the schematic representation of the helical trigonal Se structure [18].

of the lattice defects reaches a critical value, the ordered $[-\text{Se}]_n$ molecular chains turned into the disordered $[-\text{Se}]_n$ polymeric chains, that is, the SSA of t-Se occurs. However, the systematic investigation on the local structure evolution of Se intra-chain (such as the coordination number and bond length, etc.) during the MM-induced SSA process is still lacking.

In present work, extended X-ray-absorption fine-structure (EXAFS) was employed to investigate the local structural evolution of the selenium samples during the MM-induced amorphization process. In addition, the structure of the am-Se is compared with that of the as-quenched amorphous Se (aq-Se), which was investigated previously [22].

2. Experimental

2.1. Sample preparation

Mechanical milling of commercial elemental Se powder (with a purity of 99.999% and particle size smaller than 600 mesh) was carried out in a high-energy vibratory ball mill at ambient temperature. The milling media were hardened steel balls and vial. About 4.5 g Se powders were charged into the vial with a ball-to-powder weight ratio of 10:1, and were sealed, to avoid oxidation, by an elastic O-ring in a stationary dry Ar atmosphere (O_2 , $\text{H}_2 < 5$ ppm) with an over-pressure about 3 atm. Each mechanical milling procedure was started with a new dose of initial powders and was carried out without interruption. Previous XRD and differential scanning calorimetry (DSC) analyses indicated that the amorphization of crystalline Se starts when the milling time (t_m) is 30 min, as shown in Fig. 1. During the period of $t_m = 30\text{--}120$ min, the amorphous

Se fraction increases in a linear relation, and then tends slowly to 100% at 250 min [20]. Wet chemical analysis and energy-dispersive X-ray analysis indicated that, in the sample milled for 250 min, the oxygen content is less than 0.1 wt% and the iron content less than 0.02 wt%.

2.2. EXAFS measurements

EXAFS measurements were carried out at the beam-line 4W1B (with an energy range of 3.5–22 keV) of Beijing Synchrotron Radiation Facility for High Energy Physics. The storage ring current was 50–80 mA at a photon energy of 2.2 GeV. The continuous wavelength X-ray beam, with an energy resolution of ~ 2 eV at 9 keV, was provided by a directly water-cooled Si(111) double crystal monochromator. Taking care of the severe requirements of thickness and homogeneity for the accurate absorption measurements, the milled Se powders were spread uniformly on the special translucent adhesive tape for EXAFS measurements. The X-ray absorption coefficient at Se K-edge was measured using transmission mode at room temperature by the ion chamber detectors. In order to minimize the absorption of high-energy X-ray harmonics, the monochromator was detuned about 30%, and the ion chamber monitoring the incident X-ray beam was filled with argon and that monitoring the transmitted X-ray beam filled with a mixture of argon (75 vol.%) and nitrogen (25 vol.%).

3. Results

Fig. 2 shows the measured K-edge X-ray-absorption spectra for the Se samples subjected to different milling periods. This figure shows an excellent signal-to-noise ratio. With increasing incident X-ray energy, the K-edge absorption coefficients of all measured Se samples increase sharply to maxima at Se K-absorption edge, E_0 , arising from the transfer of electron from 1s to 4p orbital, and then exhibit periodic oscillations when the X-ray energy is larger than E_0 .

Since the oscillatory part of the X-ray-absorption spectra in the post-K-edge region (e.g. EXAFS) contains the atomic local structural information, we isolated the X-ray-absorption fine-structure from the absorption spectra and inverted it to obtain the structural parameters (e.g. coordination number, bond length, etc.). Details of the procedure are given in Refs. [23,24]. Here we only outline the procedure. Firstly, the curve $a_1E^{-3} + a_2E^{-4} + a_3$, with photon energy E and parameters a_1 , a_2 , and a_3 , was fitted to the smooth background caused by the atomic absorption in the pre-K-edge region. Another least-square spline was fitted with the background in the post-edge region. The thickness parameter t was determined by equating the difference of the two polynomial curves to $t \cdot (C \cdot E^{-3} - D \cdot E^{-4})$

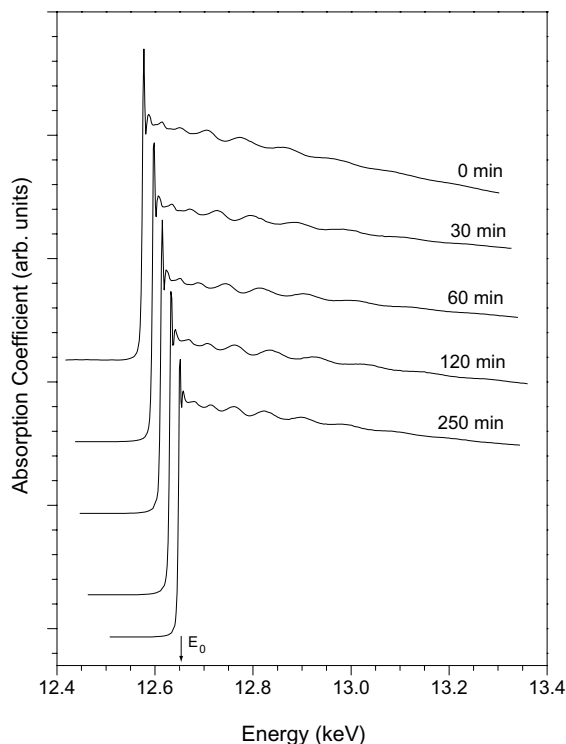


Fig. 2. Se K-edge X-ray absorption spectra for the milled Se samples with different milling times (as indicated), the upper spectrum shifts about 20 eV toward the lower X-ray energy compared to the lower spectrum.

where C and D were given in Ref. [25], at a fixed point near K-edge. The EXAFS χ (defined in the section of Appendix A) was derived by removing the least-square spline from the absorption spectra and subsequently by normalizing by $t \cdot (C \cdot E^{-3} - D \cdot E^{-4})$. The data after background removal and normalization were then converted to a function of the photoelectron wave number k , rather than as a function of energy. The conversion is $k = (2m(E - E_0)/\hbar^2)^{1/2}$, where E_0 was chosen at the top of the first peak in the absorption spectra in all samples and m is the electron mass. The converted EXAFS oscillations multiplied by k^3 , $k^3\chi(k)$, of the milled Se samples are shown in Fig. 3.

In order to get the detailed information about the influence of milling process on the $[-\text{Se}-]_n$ molecular chains, the oscillatory EXAFS, $k^3\chi(k)$, was converted from a representation in terms of photoelectron wave number to that in coordinate space by the Fourier transform [23,24] in the region from 3.0 to 15.3 \AA^{-1} . The Fourier transform gives an immediate and graphic presentation of how many coordination shells are contributing to the EXAFS signal and their approximate distances. Typical results for the magnitude of the Fourier transformation, $FT(k^3\chi(k))$, for the milled Se samples are shown in Fig. 4. The Fourier transformation from all milled Se samples only contain a prominent peak, which was observed at about 2 \AA and corresponds

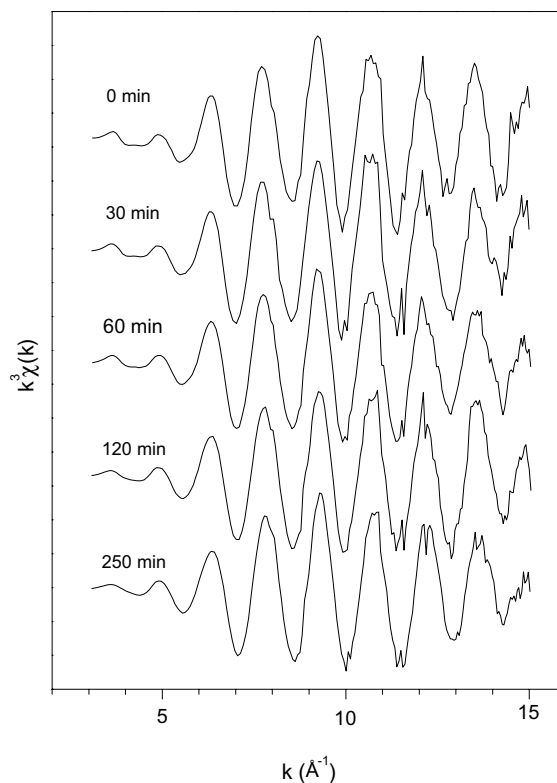


Fig. 3. Se K-edge EXAFS oscillations, $k^3\chi(k)$, for the milled Se after background removal and normalization plotted as a function of photoelectron wave number k .

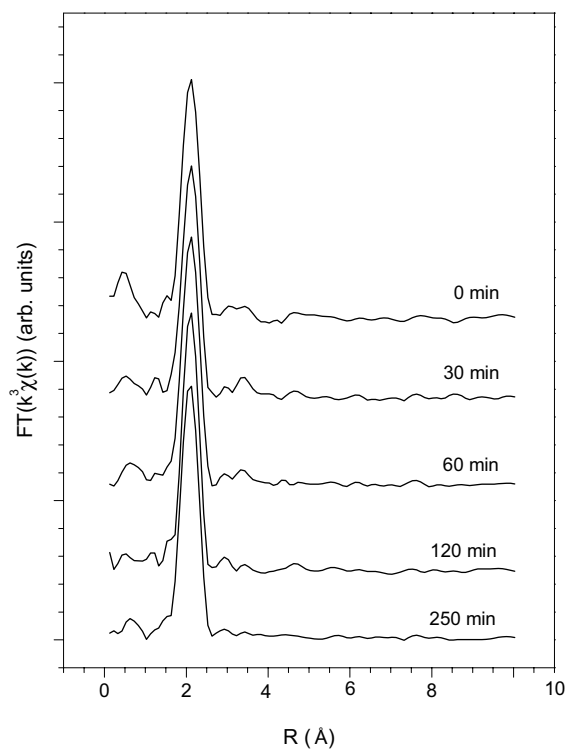


Fig. 4. Magnitude of Fourier transform of Se K-EXAFS oscillations multiplied by k^3 , $FT(k^3\chi(k))$, for the milled Se. The transform range was from 3.0 to 15.3 \AA .

Table 1

A listing of the coordination number, bond length, and Debye–Waller factor of the first coordination shell for the milled Se samples, as-quenched amorphous Se (aq-Se) [22] and crystalline t-Se [26]

Milling time (min)	Coordination number (Se–Se)	Bond length (Å)	Debye–Waller factor (Å ²)
0	2.01	2.373	0.0181
10	2.13	2.370	0.0192
20	2.09	2.369	0.0186
25	2.18	2.368	0.0202
30	2.13	2.367	0.0194
40	2.12	2.366	0.0204
60	2.11	2.365	0.0210
90	2.06	2.363	0.0207
120	2.09	2.353	0.0211
200	2.00	2.353	0.0206
250	1.95	2.341	0.0210
aq-Se [22]	2.14 ± 0.03	2.35 ± 0.01	0.016 ± 0.001
t-Se [26]	2.0	2.37	–

The error bars are estimated to be 0.03, 0.01 Å and 0.001 Å² for the coordination number, bond length, and Debye–Waller factor of the first coordination shell, respectively.

to the signal of first-coordination shell (A–B bond in Fig. 1), e.g. the intra-chains first-nearest neighboring selenium atoms. The peaks due to the second-nearest coordination sphere (A–B* bond in Fig. 1, the inter-chains first-nearest neighboring Se atoms) and the third-nearest coordination sphere (A–C bond, the intra-chain second-neighboring Se atoms) were not found for the milled samples in present EXAFS experiment, which was performed at room temperature. In literature, low temperature EXAFS observed the second- and third-nearest neighboring peaks of the crystalline Se at about 3.3 and 3.7 Å, respectively [26].

Since the Fourier transformation from the milled Se samples contain only the signal of the first-coordination shell, we can only calculate the structural parameters of the first shell. The Fourier-transformed data with the contribution of the first coordination shell were back Fourier transformed into k space, then fitted by the least-square curve based on the single scattering theory [27]. The curve fitting results were listed in Table 1 and plotted in Fig. 5(a)–(c). From Fig. 5(a), at the early stage of milling, the coordination number, N , increases from 2.01 ± 0.03 ($t_m = 0$ min) to a maximum value of 2.18 ± 0.03 (25 min), when $t_m \geq 30$ min, N decreases gradually down to about 1.95 ± 0.03 (250 min). The N value of the am-Se is much smaller than that of the aq-Se, which was reported as $N_{aq-Se} = 2.14 \pm 0.03$ [22]. The N of the unmilled Se sample is comparable to that of the literature value (about 2) [26].

From Fig. 5(b), during the whole milling process, the bond length, l , of the milled Se samples decreases gradually from about 2.37 ± 0.01 Å (0 min) to 2.34 ± 0.01 Å (250 min). The reduction amplitude is larger than the experimental uncertainty. The bond length of the am-Se (2.34 ± 0.01 Å) is comparable to that of the aq-Se ($l_{aq-Se} = 2.35 \pm 0.01$ Å). In Refs. [22,28], the bond length of the crystalline Se is reported to be 2.36 ± 0.01 and 2.37

Å, which agree with the value of the unmilled Se sample. The bond length of t-Se has the following relation with the lattice parameters a and c [19]:

$$l^2 = (c/3)^2 + (ma)^2. \quad (1)$$

Therefore, according to Eq. (1), with $l_0 = 2.374$ Å, $a_0 = 4.3662$ Å, $c_0 = 4.9536$ Å, ($m = 0.3903$) and the measured lattice parameters, the l of t-Se in the milled Se powder can be calculated. The lattice parameters a and c of the t-Se in the milled Se powder were calculated from XRD peak centroid positions [29] and were reported in Ref. [20]. The calculated l of t-Se in the milled Se powder was also shown in Fig. 5(a). The bond length of t-Se keeps nearly unchanged during the whole milling process and agrees with the standard value ($l_0 = 2.373$ Å) in literature [19]. Since the bond length from the EXAFS measurements is the average of both t-Se and amorphous Se, the decreased bond length from EXAFS suggests the shortened bond length of the as-milled amorphous Se compared to that of t-Se.

From Fig. 5(c), during the whole milling process, the Debye–Waller factor increases from 0.018 ± 0.001 Å² (0 min) to 0.021 ± 0.001 Å² (250 min). The Debye–Waller factor of the unmilled Se sample is comparable to the value of crystalline Se in Ref. [22]. However, the Debye–Waller factor of the am-Se (0.021 ± 0.001 Å²) is much larger than that of the aq-Se ($\sigma_{aq-Se}^2 = 0.016 \pm 0.001$ Å² [22]).

4. Discussion

The above results demonstrate that the mechanical milling process changed the intra-chains structural parameters. During the grain-refinement (0–30 min), the nearest-neighboring coordination number and Debye–Waller parameter of the intra-chains increase

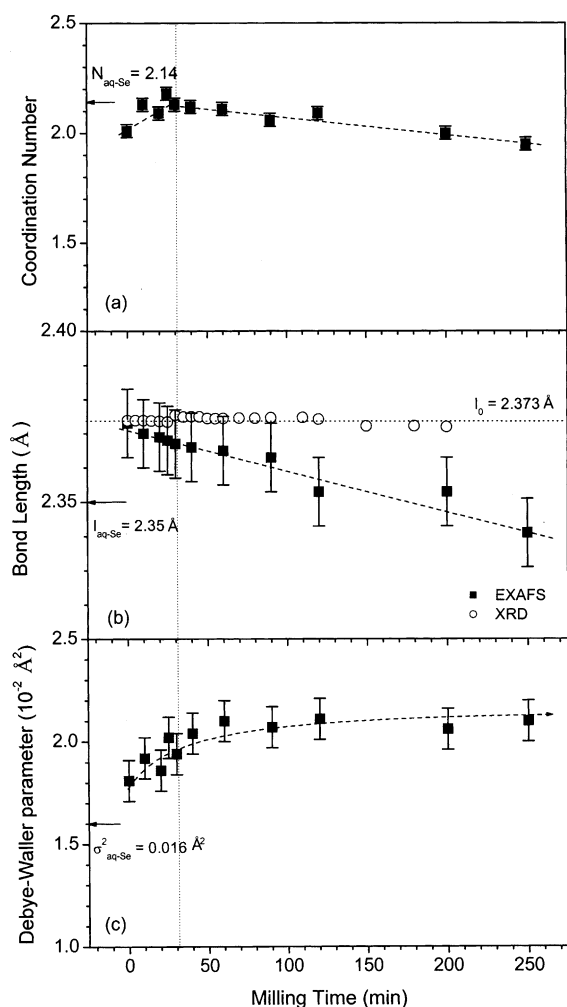


Fig. 5. Milling time dependences of the coordination number (a), the bond length (b), and the Debye-Waller factor (c) of the first coordination shell for the milled Se samples. The vertical dotted line indicates the amorphization onset ($t_m = 30$ min), and the horizontal dotted line in Fig. 5(b) indicates the standard bond length ($l_0 = 2.373$ Å) in literature [19]. The other dashed lines are guides to the eye for the variations of the coordination number, bond length and Debye-Waller parameter, respectively.

(Fig. 5(a),(c)), and during the amorphization process (30–250 min), the nearest-neighboring coordination number and coordination distance of the intra-chains decrease (Fig. 5(a),(b)). In addition, previous XRD measurements indicated that the lattice parameter a of

the milled Se (the distance between the neighboring $[-Se-]_n$ chains) increased against the milling time during the grain-refinement and kept unchanged during SSA process [20]. This result suggests that the MM process weakens Se inter-chain interaction during the grain refinement. The increased lattice parameter a was mainly originated from the strong interaction between the numerous grain boundaries and nanometer-sized crystallites, which was verified in Ref. [29]. When $t_m = 30$ min, the grains were refined to the minimal value [20], and the lattice parameter a was increased to the critical values where the ordered $[-Se-]_n$ chains can be destabilized to the disordered chains. During the SSA process ($t_m > 30$ min), the $[-Se-]_n$ chains, of which the inter-chain coordination distance was activated to the critical values, continuously destabilized into the disordered chains. The preferential destruction of inter-chain bonds can be qualitatively understood by the fact that the inter-chain Van der Waals force is much weaker than the intra-chain covalent bond.

The increase of N during the grain-refinement ($t_m < 30$ min, Fig. 5(a)) can be ascribed to the threefold-coordinated sites. During the grain refinement, the MM process induced large amount of defects (grain boundaries, points defects, etc.) into the lattice, which can excite the electrons from the top of the valence band, formed by lone pair (LP) electrons, into the conduction band leaving one electron in the former LP orbital. If the distance between such excited atoms is close to the covalent bond length and the spins have opposite directions, additional covalent bonds can be dynamically formed between excited atoms, making a part of selenium atoms threefold-coordinated, as schematically represented in Fig. 6. During the SSA process when $t_m \geq 30$ min, the additional covalent bonds formed between $[-Se-]_n$ molecular chains are destroyed resulting in the decreased N . Infrared and Raman spectroscopy measurements revealed that the as-quenched amorphous Se is mainly composed of Se_8 ring and $[-Se-]_n$ polymeric chains [21]. The formation of higher-than-twofold-coordinated sites may result in the observed larger $N (= 2.15 \pm 0.03)$ of the aq-Se than that of the as-milled one. Further investigation on the electronic properties of the milled Se and aq-Se will be performed to understand the variation of N .

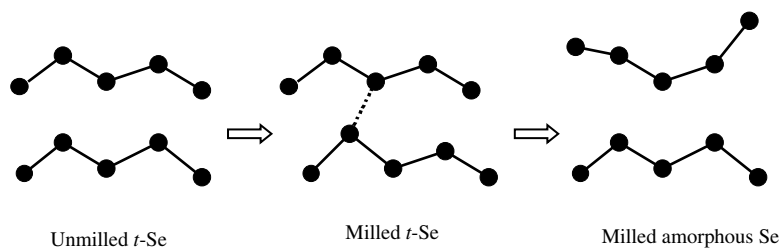


Fig. 6. A schematic diagram of the local structural change in selenium chains as a result of mechanical milling. The dashed line between the two $[-Se-]_n$ molecular chains of the milled t -Se is the interchain covalent bond which forms the threefold-coordinated sites.

The bond length shortening during SSA process can be understood by the destroyed inter-chain interaction due to MM. The helical chain structure in t-Se originates from minimization of the intra- and inter-chain repulsive interactions. The MM process destroys the inter-chain interaction, therefore, the intra-chain interaction was strengthened in order to reach the new stable state. On the other hand, the structural disorder in the amorphous Se relaxes the folded spiral chain. As a result of decreased Coulomb repulsion, this would increase the overlap integral, or the bond charge, shortening the bond length.

As mentioned above, the formation of new inter-chain bonds is expected to introduce a local distortion around the threefold-coordinated sites, which would result in an increase in the Debye–Waller factor. Moreover, the lattice imperfections induced by MM also can result in the increase of Debye–Waller factor. The evidently larger Debye–Waller factor of the am-Se than that of the as-quenched one suggests that there exist more defects in the am-Se, which was verified by the fact of the lower crystallization temperature and enthalpy of the as-milled amorphous Se compared to those of the as-quenched one [30].

5. Conclusion

In summary, EXAFS measurements were performed on the solid-state amorphization of trigonal Se induced by mechanical milling. During the amorphization process, the first-nearest neighboring coordination distance and the coordination number were found to decrease with the milling time, while the Debye–Waller factor increases, suggesting that the MM results in the strengthening of intra-chain and weakening of inter-chain interactions. Compared to the structure of the as-quenched amorphous Se, the coordination number of the as-milled amorphous Se become smaller, while the Debye–Waller factor becomes larger, which is caused by the milling process.

Acknowledgements

Financial support from the Chinese Academy of Science and the National Science Foundation of China (Grant Nos. 59625101 and 59431021) are acknowledged.

Appendix A

The extended X-ray-absorption fine-structure (EXAFS) $\chi(k)$ is the oscillation in the absorption coefficient on the high-energy side of X-ray absorption edges, which can extend around 1000 eV past the edge. If the multiple-scattering effects between atoms are ne-

glected (single scattering), then $\chi(k)$ can be expressed as (for details see Refs. [23,24]):

$$\chi(k) = \frac{m}{4\pi\hbar^2k} \sum_j \frac{N_j}{R_j^2} t_j(2k) e^{-2R_j/\lambda} e^{-2k^2\sigma_j^2} \times \sin[2kR_j + \delta_j(k) + \phi_j(k)],$$

where k is the wave vector of the ejected photoelectron, m is the mass of X-ray photoelectron, \hbar is the Planck's constant, j is the j th neighboring coordination shell of the absorbing atom, N_j is the number of atoms contained in the j th coordination shell, R_j is the average position between the origin atom and the j th atom, $t_j(2k)$ is the magnitude of the amplitude for backscattering from the j th atom, λ is the mean free path for electron–electron and other inelastic scatterings, σ_j is the root mean square deviation from R_j , $\delta_j(k)$ is the phase shift in the absorbing atom potential and $\phi_j(k)$ is the phase shift in the back-scattering amplitude of the j th atom.

References

- [1] C. Suryanarayana, Prog. Mater. Sci. 46 (2001) 1.
- [2] W.L. Johnson, Prog. Mater. Sci. 30 (1986) 81.
- [3] R.B. Schwarz, C.C. Koch, Appl. Phys. Lett. 49 (1986) 146.
- [4] E. Hellstern, L. Schultz, Mater. Sci. Eng. 97 (1988) 39.
- [5] L. Schultz, J. Less-Comm. Met. 145 (1988) 233.
- [6] A.W. Weeber, H. Bakker, Physica B 153 (1988) 93.
- [7] A.Ye. Yermakov, Ye.Ye. Yurchikov, V.A. Barinov, Phys. Met. Metall. 52 (1981) 50.
- [8] C. Polistis, W.L. Johnson, J. Appl. Phys. 60 (1986) 1147.
- [9] E. Gaffet, N. Merk, G. Martin, J. Bigot, J. Less-Comm. Met. 145 (1988) 251.
- [10] J.S.C. Jang, C.C. Koch, J. Mater. Res. 5 (1990) 498.
- [11] Y.S. Cho, C.C. Koch, J. Alloys Comp. 194 (1993) 287.
- [12] E. Gaffet, M. Harmelin, J. Less-Comm. Met. 157 (1990) 201.
- [13] T.D. Shen, C.C. Koch, T.L. McCormick, R.J. Memanich, J.Y. Huang, J.G. Huang, J. Mater. Res. 10 (1995) 139.
- [14] J.Y. Huang, H. Yasuda, H. Mori, Philos. Mag. Lett. 79 (1999) 305.
- [15] E. Gaffet, Mater. Sci. Eng. A136 (1991) 161.
- [16] T. Fukunaga, M. Utsumi, H. Akatsuka, M. Misawa, U. Mizutani, J. Non-Cryst. Solids 205–207 (1996) 531.
- [17] G.J. Fan, F.G. Guo, Z.Q. Hu, M.X. Quan, K. Lu, Phys. Rev. B55 (1997) 11010.
- [18] H.M. Isomäki, J. von Boehm, Phys. Rev. B35 (1987) 8019.
- [19] P. Ungar, P. Cherin, in: C.W. Cooper (Ed.), The Physics of Selenium and Tellurium, Pergamon, Oxford, 1969, p. 223.
- [20] Y.H. Zhao, Z.H. Jin, K. Lu, Philos. Mag. Lett. 79 (1999) 747.
- [21] F.Q. Guo, K. Lu, Phys. Rev. B57 (1998) 10414.
- [22] Y.H. Zhao, K. Lu, T. Liu, Phys. Rev. B59 (1999) 11117.
- [23] E.A. Stern, D.E. Sayers, F.W. Lytle, Phys. Rev. B11 (1975) 4836.
- [24] E.A. Stern, S.M. Heald, in: E.E. Koch (Ed.), Handbook of Synchrotron Radiation, 1B, North-Holland, Amsterdam, 1983 [Chapter 10].
- [25] C.H. Macgillavry, C.D. Riech, K. Lonsdale, in: Int. Tables for X-ray Crystallography, 3, The Kynoch, UK, 1972.
- [26] A.V. Kolobov, H. Oyanagi, K. Tanaka, Ke. Tanaka, Phys. Rev. B55 (1997) 726.
- [27] E.A. Stern, Phys. Rev. B10 (1974) 3027.
- [28] D. Hohl, R.O. Jones, Phys. Rev. B43 (1991) 3856.
- [29] Y.H. Zhao, K. Zhang, K. Lu, Phys. Rev. B56 (1997) 14322.
- [30] F.Q. Guo, K. Lu, Philos. Mag. Lett. 77 (1998) 181.